AGU ADVANCING EARTH AND SPACE SCIENCES

Geophysical Research Letters

RESEARCH LETTER
10.1029/2026GL124017

Tracing the Abyssal Water Pathways in the Indian Ocean

Kaushik Mishra[1], Bishakhdatta Gayen[1,2], Kathryn L. Gunn[3], P. N. Vinayachandran[1,4], and Nihar Paul[5,6]

[1]Centre for Atmospheric and Oceanic Sciences, Indian Institute of Science, Bengaluru, India, [2]Department of Mechanical Engineering, The Australian Centre for Excellence in Antarctic Science, University of Melbourne, Melbourne, VIC, Australia, [3]School of Ocean and Earth Science, University of Southampton, Southampton, UK, [4]Divecha Centre for Climate Change, Indian Institute of Science, Bengaluru, India, [5]Department of Physical Oceanography, Woods Hole Oceanographic Institution, Woods Hole, MA, USA, [6]School of Climate Change and Sustainability, Azim Premji University, Bengaluru, India

Key Points:

- High-resolution regional model, reanalyses, and observation data sets reveal the critical pathways of abyssal watermasses in the Indian Ocean
- Approximately 12.5 Sv of abyssal waters enter the Indian Ocean through three pathways, of which about 10 Sv upwells along key hotspots
- Of the 10 Sv of upwelled abyssal waters, 8 Sv forms a southward return flow as deep waters at shallower depths

Supporting Information:

Supporting Information may be found in the online version of this article.

Correspondence to:

B. Gayen,
bishakhdatta.gayen@unimelb.edu.au

Citation:

Mishra, K., Gayen, B., Gunn, K. L., Vinayachandran, P. N., & Paul, N. (2026). Tracing the abyssal water pathways in the Indian Ocean. *Geophysical Research Letters*, *53*, e2026GL124017. https://doi.org/10.1029/2026GL124017

Received 27 APR 2026
Accepted 25 JUN 2026

Author Contributions:

Conceptualization: Kaushik Mishra, Bishakhdatta Gayen, Kathryn L. Gunn
Data curation: Kaushik Mishra
Formal analysis: Kaushik Mishra
Funding acquisition: Bishakhdatta Gayen
Investigation: Bishakhdatta Gayen, Kathryn L. Gunn
Methodology: Kaushik Mishra, Kathryn L. Gunn
Resources: Bishakhdatta Gayen
Software: Kaushik Mishra, Nihar Paul
Supervision: Bishakhdatta Gayen, Kathryn L. Gunn, P. N. Vinayachandran
Validation: Kaushik Mishra
Visualization: Kaushik Mishra
Writing – original draft: Kaushik Mishra, Bishakhdatta Gayen, Kathryn L. Gunn

Abstract

Antarctic-origin abyssal waters occupy a significant fraction of the global ocean volume and play a key role in deep circulation and ventilation, yet their volume is declining rapidly in a warming climate. Although the Indian Ocean (IO) contains a substantial fraction of these waters, abyssal pathways and upwelling in the basin remain poorly understood due to sparse observations. Here, we investigate abyssal transports using an eddy-resolving regional ocean model. We find the abyssal waters flooding the IO along three distinct pathways with a net northward transport of ∼12.5 Sv across 32°S, consistent with observational estimates. For the first-time, we identify regional hot-spots of large-scale abyssal upwelling that occur along ridges and continental boundaries, transferring ∼10 Sv of abyssal waters upward, of which ∼8 Sv returns southward as deep waters. These results provide new constraints on the structure and closure of the lower limb of the IO overturning circulation.

Plain Language Summary

The abyssal water occupies a significant volume of the world's oceans. The movement of abyssal water is slow, occurring on centennial to millennial time scales, but it plays an important role in transporting watermasses, nutrients, and ventilating heat and gases. The Indian Ocean (IO) houses the largest fraction of the global abyssal water volume compared to its size. In addition to insufficient measurements, there have been relatively few modeling efforts to study the abyssal transports. Therefore, we used an eddy-resolving regional ocean model, reanalyses, and observation data sets to assess the circulation of abyssal waters. We find that abyssal waters enter through the southern boundary of the IO, adjoining the Southern Ocean, along three unique pathways that flood the IO. We also quantify the vertical transport along specific sub-regions within the IO domain. These sub-regions act as "hot spots" for the abyssal water upwelling, where a large fraction of the upwelled waters are transformed into deep waters and return southward as part of the basin-scale overturning circulation. In a warming climate scenario, when the abyssal water volume is projected to contract at an alarming rate, these pathways could play an important role in modulating the future ocean state.

1. Introduction

The Meridional Overturning Circulation (MOC) is a key component of the climate system, redistributing heat, salt, carbon, and nutrients across ocean basins (Richardson, 2008). It is driven by meridional buoyancy gradients arising from temperature and salinity distributions, as well as by mechanical forcing from winds and tides (Butler et al., 2016; Cessi, 2019; Kuhlbrodt et al., 2007; Munk & Wunsch, 1998). One of its major branches passes through the Indian Ocean (IO), which, unlike the Atlantic, is constrained by its northern land boundary, prohibiting high-latitude deep-water formation. Instead, IO relies on abyssal waters sourced from the Southern Ocean, which enter the basin at depths below 2000 m (Figure 1) and ventilate its deep layers (Johnson, 2008). These waters play a critical role in setting the thermohaline structure and biogeochemical distributions of the basin, while also acting as a reservoir for anthropogenic carbon (Mahieu et al., 2020; Silvano et al., 2023). Although these abyssal waters play a central role in global overturning circulation, their pathways and basin-scale circulation within the IO remain poorly understood.

The abyssal waters are composed of Antarctic Bottom Water (AABW) and Lower Circumpolar Deep Water (LCDW), which together form the northward-propagating lower limb (depth ≥ 3500m; $\sigma_2 \geq 37.1$ kg m^{-3}) of the overturning circulation (Mantyla & Reid, 1995; Sloyan & Rintoul, 2001). AABW, the coldest ($\theta \leq -0.2$°C) and

Writing – review & editing: Kaushik Mishra, Bishakhdatta Gayen, Kathryn L. Gunn, P. N. Vinayachandran, Nihar Paul

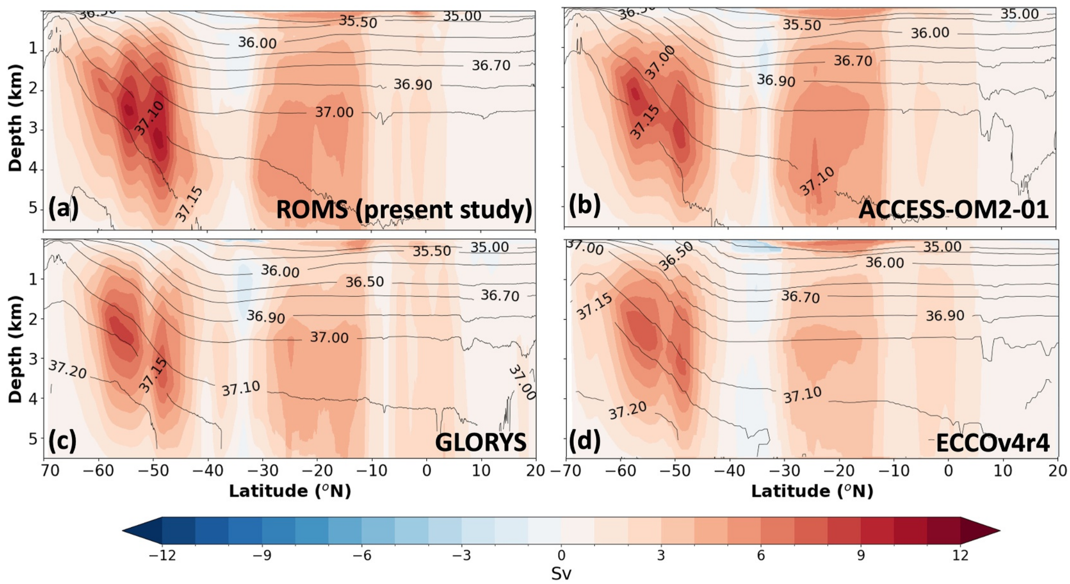

Figure 1. Panels (a–d) present the time-mean overturning streamfunction ($\overline{\psi}$; Sv) across different models in depth–latitude coordinates, calculated from the Helmholtz decomposition of the meridional velocity field. The contour lines indicate the zonally averaged potential density (σ_2) at different depths, helping to identify key water masses and illustrate the latitudinal density structure. Positive values of ψ denote counter-clockwise circulation, and negative values clockwise.

densest ($\sigma_2 \geq 37.13$ kg m^{-3}) watermass (Figure 2c), is formed along Antarctic continental margins through sea-ice-driven convection and subsequently ventilates the global abyss (Aguiar et al., 2017; Foster & Carmack, 1976; Gordon, 2009; Solodoch et al., 2022). In contrast, LCDW ($\sigma_2 \geq 37.1$ kg m^{-3}) arises from the mixing of AABW with North Atlantic Deep Water (NADW), representing a modified and slightly lighter component of the abyssal layer (Onken, 1995; van Aken et al., 2004). Recent hydrographic observations indicate that the Southern Ocean limb of these abyssal waters is undergoing rapid transformation, characterized by pronounced warming, freshening, and a decline in volume since the late 1990s (Aoki et al., 2005; Gunn et al., 2023; Johnson & Purkey, 2024; Purkey & Johnson, 2010; Rintoul et al., 2026). These changes have the potential to alter abyssal stratification, circulation pathways, and overturning strength, with implications for sea level rise, ocean heat uptake, and climate variability on multi-decadal timescales (Bindoff & Hobbs, 2013; Haynes et al., 2020; Purkey & Johnson, 2013), highlighting the need to better resolve their pathways and large-scale circulation patterns.

The Indian sector of the Southern Ocean and the Indian Ocean together house a large fraction of the global abyssal volume (Johnson, 2008; Orsi et al., 2001). However, observational studies have captured only broad-scale features of these water masses, with large uncertainties in both transport and pathways arising from sparse spatio-temporal coverage (Dengler et al., 2002; Fieux & Swallow, 1988; Warren, 1974). Existing transport estimates are primarily derived from inverse box models (Ganachaud et al., 2000; Lumpkin & Speer, 2007; McDonagh et al., 2008; Robbins & Toole, 1997; Sloyan & Rintoul, 2001), which lack the resolution to identify dynamically distinct pathways and localized transformation processes. In particular, the locations, structure, magnitude, and mechanisms of abyssal upwelling within the basin remain largely unconstrained. Furthermore, the pathways by which the upwelled and modified abyssal waters return as deep flows at upper depths (1500–3500m; $\sigma_2 \sim 36.5 - 37.1$ kg m^{-3}) have been examined only along isolated transects (Sloyan & Rintoul, 2001), leaving the basin-scale structure of the abyssal-to-deep overturning loop largely unresolved. The absence of continuous observations, in contrast to the Atlantic (Ansorge et al., 2014; Johns et al., 2011; Schiermeier, 2013), further limits our ability to monitor abyssal circulation in the IO. Moreover, previous modeling studies, even at high spatial resolution, underestimate abyssal transport by 20% or more and fail to resolve topographically steered pathways that are critical for closing the IO overturning circulation (Drijfhout & Garabato, 2008; Srinivasan et al., 2009). Resolving the abyssal water pathways, transports, and transformation rates is critical for anticipating how these waters will respond to the ongoing climate change.

10.1029/2026GL124017

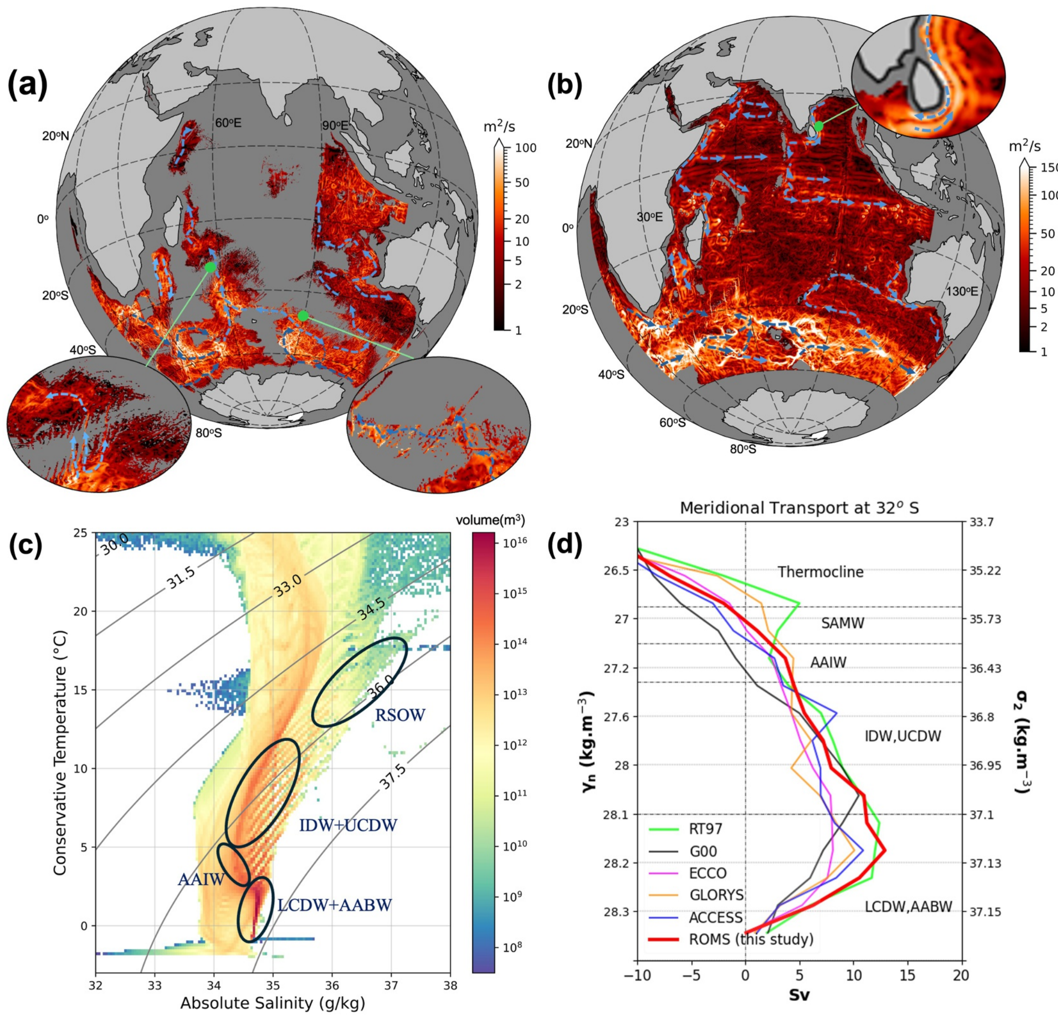

Figure 2. Time-averaged quantities are presented as follows: (a) Abyssal layer (LCDW-AABW) transport ($\overline{\mu}$), with insets focusing on two specific regions: the South-West Indian Ridge (left inset) and the Kerguelen St.Paul Island passage (right inset); (b) Deep layer (UCDW-IDW) return transport, with inset focusing on the northern Indian ocean cross basin exchange. Both panels (a, b) are displayed on a non-linear color scale to capture the full dynamic range of transport magnitudes, with colorbar ticks graded at every 5 m^2/s interval. (c) Temperature–Salinity (T–S) diagram colored by volume (m^3) and overlaid with potential density (σ_2) contours, highlighting the major water masses in the Indian Ocean (IO). Panel (d) shows the comparison of meridional transport within each density class, computed by integrating meridional velocity upward from the seafloor, along 32°S across the four models (ROMS in thick red line), with these results also compared against the inverse-box model derived transports from Robbins and Toole (1997) (RT97) and Ganachaud et al. (2000) (G00). To be consistent with the observations spanning November–January 1987, we use the November-January climatologically averaged transport for all four models.

In this present work, using a terrain-following, eddy-resolving ocean model, we resolve the major topographically steered abyssal inflow pathways in the IO and quantify their contributions to basin-scale circulation. Model outputs are evaluated against reanalyses and observational data sets. We identify key regions of abyssal upwelling and show how these modified waters reorganize into a coherent basin-scale return flow as upper-layer deep waters (1,000–3,500 m). Together, these results provide a mechanistic framework linking abyssal inflow, transformation, and return flow, demonstrating a dynamically consistent closure of the lower limb of the IO overturning circulation.

2. Data and Model Setup

For this study, we chose the Regional Ocean Modeling System (ROMS) because it uses a terrain-following vertical coordinate, which is better suited for bottom-layer flows (Ezer & Mellor, 2004; Pacanowski & Gnanadesikan, 1998; Tang & Roberts, 2005; Winton et al., 1998). The model is also coupled with an active sea-ice model. The initial configuration (first branch) is performed at a horizontal resolution of 0.25° with 75 σ-levels. The model domain extends from 5°E–155°E and 80°S–30°N, encompassing the Indian Ocean and its Southern Ocean sector. Open boundaries are prescribed along the eastern and western zonal edges of the model domain. The eastern boundary includes the Southern Ocean sector and the Indonesian Throughflow (ITF) passage within the North Australian Basin. The western boundary extends into the Atlantic sector to ensure a realistic representation of the Agulhas region. Initial temperature and salinity fields are prescribed using the World Ocean Atlas (WOA-23; 2005–2014 climatology). Boundary nudging employs a combination of WOA-derived geostrophic velocities and Ekman transport. The ocean model uses the Mellor Yamada 2.5 (Mellor & Yamada, 1982) turbulence closure scheme for vertical mixing parameterization. The model is initialized from rest and integrated for 60 years to achieve quasi-equilibrium. A second, eddy-resolving configuration (0.1°) is then branched from this equilibrated state and integrated for an additional 50 years.

The overturning circulation is compared across three different ocean products: (a) ECCOv4r4 (Forget et al., 2015); (b) GLORYS-12 (Jean-Michel et al., 2021); and (c) ACCESS-OM2-01 (Kiss et al., 2020). ECCOv4r4 and GLORYS-12 are two ocean reanalyses that involve data assimilation from observational data. ACCESS-OM2-01 is an eddy-resolving global ocean-sea ice model. Since our study focuses on the time-mean behavior of the circulation, we have considered the climatological averaging for the duration 1st January 2000 to 1st January 2015 amongst the two reanalysis products and the last 15-year averaging of ACCESS-OM2 and ROMS climatological simulations.

The meridional overturning stream function (ψ) is calculated using the potential density referenced to 2,000 dbar (σ_2) as the preferred vertical coordinate.

$$\psi(\sigma_2, y, t) = \int_{west}^{east} \int_{z=h_{\sigma_2}}^{z=0} v_{\psi}(x, y, z, t)\, dz\, dx \tag{1}$$

where v_{ψ} is the non-divergent component of the meridional velocity, and x, y, and h_{σ_2} represent the directions corresponding to longitudes, latitudes, and depth of each isopycnal layer, respectively.

The bottom (AABW-LCDW) and the overlying deep layer (the combined Indian Deep Water [IDW] and the Upper-Circumpolar Deep Water [UCDW]) transports (μ) are computed as the product of horizontal velocity and layer thickness. The definition of layer thickness differs between the Southern Ocean and the Indian Ocean sectors. North of 45°S, the bottom-layer thickness is defined as the vertical distance from the seafloor to the 37.1 kg m^{-3} isopycnal surface. South of 45°S, where isopycnals outcrop and density surfaces intersect the surface, the bottom-layer thickness is instead defined from the seafloor up to a fixed depth of 3,000 m. For the deep (IDW-UCDW) layer, the thickness is defined as the vertical distance between the 37.1 kg m^{-3} and 36.5 kg m^{-3} isopycnal surfaces at each grid point. Further details regarding the model setup and transport calculations are provided in (Texts S1–S4, Figures S2–S8, Table T1 in Supporting Information S1).

3. Results

We examine the overturning circulation, the abyssal water pathways, and vertical transports in a climatological framework, using the final 15 years of the equilibrated model output. The following section describes the zonally integrated IO circulation as inferred from the time-mean meridional overturning streamfunction ($\overline{\psi}$). We then examine the abyssal water pathways using the volume-transport framework $(\overline{\mu})$. Finally, we analyze the dynamics of abyssal upwelling based on vertical volume flux and the associated return-flow pathways of the transformed waters within the overlying deep layer.

3.1. IO Time-Mean Overturning Circulation

The time-mean Indian Ocean meridional overturning circulation (IO-MOC; $\overline{\psi}$) exhibits a single counter-clockwise cell that spans the basin from ∼100 m depth to the seafloor (Figures 1a–1d), resembling the Pacific overturning circulation (Talley, 2013) but contrasting with the two-celled structure of the Atlantic (Lumpkin & Speer, 2007). This structure is primarily associated with the abyssal density range ($\sigma_2 \approx 37.1 - 37.15$ kg m^{-3}), highlighting the dominant role of Southern Ocean–sourced abyssal waters in governing the IO overturning circulation. The single-celled structure is robust across all models (Figures 1a–1d), with maximum overturning strength of ∼12.4 Sv south of 40°S. In the subtropical IO, the overturning weakens and exhibits a vertically separated structure—a stronger abyssal cell (∼6.3 Sv below 1,000 m) and a weaker upper cell (∼2–3 Sv above 700 m). As the circulation extends northward, its magnitude decreases substantially, reflecting the combined influence of Southern Ocean inflow, regional wind forcing, equatorial zonal flows, and basin geometry.

South of 40°S, the overturning weakens between 40°S and 35°S under the influence of the Antarctic Circumpolar Current and a wind-driven Deacon cell (∼1 Sv). In the tropical IO, the Indonesian Throughflow (ITF; ∼10 Sv into the basin) primarily contributes to zonal transport, with its influence on $\overline{\psi}$ confined to the upper ∼300 m. Its role in ventilating intermediate layers (500–1,200 m) and its linkage to intermediate overturning have been highlighted in recent studies (Zhou et al., 2024). Below this depth, the contribution of Southern Ocean–sourced abyssal waters diminishes substantially further north. In the equatorial region, $\overline{\psi}$ further weakens (∼0.1–2 Sv; Figures 1a–1d), associated with the deep-reaching influence of seasonally reversing boundary currents, including the Findlater jet (Lee & Marotzke, 1998). In the northern IO, these seasonally reversing circulations largely cancel in the time mean, resulting in a negligible net overturning signal (<0.5 Sv).

Overall, the upper and intermediate overturning cells in the IO basin largely cancel in the annual mean due to strong seasonal reversals, resulting in a weak net contribution to the time-mean IO-MOC. Consequently, the overturning circulation is primarily governed by deep and abyssal transports (Figures 1a–1d) within the IO basin. The modeled structure of $\overline{\psi}$ is broadly consistent with observational estimates (Ganachaud et al., 2000; Robbins & Toole, 1997), which indicate a weak, predominantly single-celled overturning with ∼10–15 Sv of abyssal transport entering from the SO across 32°S transect (Figure 2d). The meridional overturning streamfunction ($\overline{\psi}$) represents a zonally integrated, two-dimensional view of the circulation. A complete understanding, therefore, requires resolving the three-dimensional pathways of abyssal inflow, which we examine in the following section.

3.2. Abyssal Water Pathways

The abyssal circulation in the Indian Ocean is governed by the combined transport of AABW and LCDW, occupying the density range $\sigma_2 \geq 37.1$ kg m^{-3} (Figure 2c). Here, we focus on their integrated transport and pathways inferred from the ROMS simulations. In the IO sector of the Southern Ocean, AABW is partly formed locally along the Amery Ice Shelf and Cape Darnley Polynya (Mensah et al., 2021), entering through Prydz Bay and contributing about 1.8 Sv to the abyssal inflow. However, this local source represents only a fraction of the total supply. A larger contribution arises from inter-basin exchange, with approximately 2.6 Sv advected eastward from the Weddell Sea into the western IO, and about 4.1 Sv supplied from the Ross Sea and Adélie Land regions into the eastern basin. These waters mix with eastward-flowing Circumpolar Deep Water (CDW; $\sigma_2 > 37.05$ kg m^{-3}) to form LCDW. The combined LCDW–AABW abyssal system (depth ≥ 3500 m) amount to ∼12.5 Sv (Figure 2d) and enter the IO through three primary, topographically guided conduits: the Perth Basin (∼44%), the Crozet Basin (∼39%), and the Mozambique Basin (∼17%) (Figures 2a and 3a; Movie S1).

The most voluminous abyssal pathway originates in the Australian–Antarctic Basin (Figure 2a), where dense AABW sourced from the Ross and Adélie Seas flows northward along the western boundary of the Kerguelen Plateau, mixing with overlying LCDW. The combined flow follows the Southeast Indian Ridge before splitting into multiple branches (Figure 2a). A minor fraction recirculates within the Australian–Antarctic Basin, while a small branch feeds the Crozet Basin through the Kerguelen–St. Paul passage. The dominant branch transports about 8.1 Sv northward into the Perth Basin, establishing it as the primary conduit of abyssal inflow into the IO basin. Of this, approximately 5.5 Sv crosses 32°S, truly entering the IO, while the remainder flows eastward into the South Australian Basin. Within the Perth Basin, the abyssal flow is strongly steered along the eastern boundary by major topographic features, consistent with observations (Sloyan, 2006) but not captured in previous modeling studies. Further downstream, the flow is guided by Broken Ridge and the Ninety-East Ridge into the

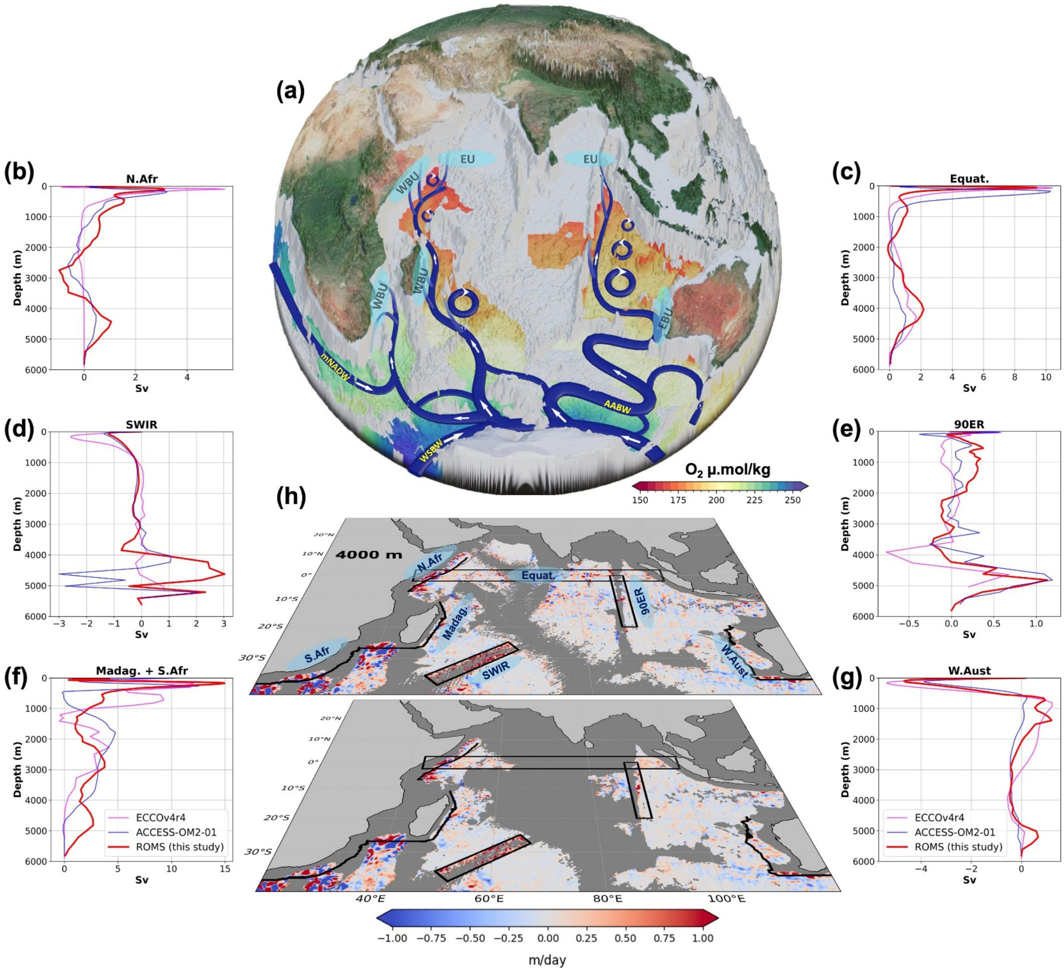

Figure 3. (a) Schematic showing the Abyssal water pathways (blue lines with white arrows) along with the upwelling hotspots (light blue shadings) representing deep Equatorial Upwelling (EU), deep Western Boundary Upwelling (WBU), and deep Eastern Boundary Upwelling (EBU). Also shown are the pathways of various watermasses contributing to the abyssal water volume (yellow texts: mNADW (modified NADW, AABW, and WSBW [Weddell Sea Bottom Water]). The background shows the dissolved Oxygen concentration (in µmol kg^{-1}) of the abyssal waters based on the World Ocean Atlas WOA23 (Garcia et al., 2024) data. Panels (b–g) display the vertical volume flux (in Sv), which is quantified by integrating the vertical velocity from each model across various regions. The regions for integration are marked by thick black lines parallel to the coast, and ±2.5° within the equator, and in the boxed regions along the Southwest Indian Ridge (SWIR) and 90 East Ridge (90ER) as shown in panel (h). The flux calculated in the regions marked by Madag., S.Afr., N.Afr., and W.Aust. is performed within the areas enclosed by the thick lines up to the coastlines at each depth level. The two layers in (h) illustrate the vertical velocity (in m/day) derived from ROMS across 4,000 m depth (top) and along the 37.1 kg m^{-3} isosurface (bottom), both Gaussian-smoothed ($\sigma = 2$ grid points).

Wharton Basin, where a cyclonic gyre traps a substantial fraction of the transport (∼4.2 Sv). Only a limited portion continues northward, with about 1.5 Sv reaching the North Australian Basin and a negligible fraction (∼0.2 Sv) crossing the equator.

The second pathway originates in the Enderby Abyssal Plain, where a cyclonic gyre around the Conrad Rise (Figure 2a) redistributes approximately 9.3 Sv of abyssal waters. Of this, about 5.2 Sv crosses the Crozet–Kerguelen gap to feed the IO branch, while approximately 1.8 Sv is diverted into the Agulhas Basin, with the remainder entering the Atlantic. A deep western boundary current in the Crozet Basin transports about 4.9 Sv along 32°S toward the Southwest Indian Ridge. However, strong topographic constraints imposed by narrow fracture zones restrict further northward propagation, causing substantial recirculation within the Crozet Basin and limiting the renewal of dense waters. Only a reduced transport (2.5 Sv) leaks into the Madagascar Basin through discrete fracture channels, where it continues northward along the Amirante Ridge system. Downstream,

10.1029/2026GL124017

much of this flow is again trapped within basin-scale recirculations, and only a small fraction (0.6 Sv) ultimately crosses the equator into the Somali Basin, highlighting the dominant control of fracture-zone topography in regulating abyssal exchange and limiting equatorward transport of abyssal waters.

The third and shortest pathway comprises a relatively weak abyssal inflow, with approximately 1.2 Sv originating from the Atlantic and about 0.9 Sv from the Agulhas Basin, together forming a northward flow along the western boundary of the Mozambique Basin. This pathway is dominated by LCDW and exhibits strong interaction with overlying southward-flowing intermediate waters. As a result, the abyssal flow undergoes significant transformation, leading to a reversal in circulation around 27°S. Much of the transport is redirected at intermediate depths (800–1,800 m) and ultimately feeds into the Agulhas Current system, highlighting strong vertical coupling between abyssal inflow and intermediate overturning within the western boundary system.

To examine abyssal circulation within the Arabian and Central Indian Basins, we analyze the bottom-intensified transport of the northward-propagating AABW-LCDW inflow. North of ~10°S, diapycnal mixing weakens the 37.1 kg m^{-3} isopycnal, and the abyssal signal manifests as bottom-following flow steered by basin topography. Thus, the 37.1 kg m^{-3} isopycnal cannot be used to quantify the abyssal transports in these basins, where we use 36.5 kg m^{-3} isopycnal criteria to classify the abyssal watermass. In the Arabian Basin, a weak anticyclonic recirculation develops, constrained by the Carlsberg Ridge and Owen Fracture Zone, while the modified abyssal waters spread laterally beneath the 36.5 kg m^{-3} surface and gradually feed into the overlying deep (IDW-UCDW) layer. A similar bottom-intensified spreading is observed in the Central Indian Basin, where the flow propagates eastward and contributes to deep-layer ventilation. Red Sea and Persian Gulf overflows (~1.5 Sv combined, RSOW ~1 Sv), though confined to intermediate depths (500–1,400 m), modify basin stratification and interact with the abyssal layer (Figure 2c). The descending RSOW plume promotes mixing at the abyssal interface, supporting upward transformation of ~1 Sv into the deep return branch and enhancing vertical exchange between intermediate and abyssal layers.

The abyssal pathways are further supported by dissolved oxygen distribution (Figure 3a), which provides a qualitative estimate of ventilation and water-mass transformation. Near their southern source regions, abyssal waters are well ventilated by AABW, as indicated by high oxygen concentrations along the Antarctic continental margins (Figure 3a). As these waters propagate northward along the seafloor, progressive mixing with overlying LCDW reduces their oxygen content. In contrast to other basins, the Mozambique Basin exhibits relatively elevated abyssal oxygen levels, consistent with a stronger influence from Atlantic-sourced waters. Across all three pathways, the systematic decline in oxygen and abyssal volume toward lower latitudes indicates limited resurfacing during transit and highlights the role of mixing-driven transformation along the pathways. These pathway-dependent transformations and their implications for abyssal-to-deep water exchange are examined further in the following section.

3.3. Quantifying the Upwelling

Abyssal waters entering the Indian Ocean must ultimately upwell to close the overturning circulation. Geostrophically constrained horizontal flow, however, breaks down near topographic boundaries and fracture zones, where ageostrophic processes permit vertical motion. In regions with sloping isopycnals, pressure gradients are generated that favor vertical transport along deep western boundaries, narrow fracture zones, and equatorial regions, while also facilitating the upward movement of water masses along isopycnal surfaces (Spall, 2024). The topographically driven mixing also plays a crucial role in the upwelling of watermasses (Mashayek et al., 2024). Consistent with this, the abyssal $\overline{\psi}$ reveals that upwelling is concentrated in distinct, topographically controlled regions rather than occurring uniformly across the basin (Figure 3h). Here, we identify six key upwelling hotspots and provide a dynamically consistent, basin-wide quantification of their magnitudes and vertical structure.

The strongest upwelling occurs in the western IO, where the convergence of major abyssal pathways creates a primary ventilation hotspot near the southern tip of Africa and along the eastern Madagascar margins. In this region, ~3.7 Sv of LCDW upwells at intermediate depths (~2,700 m), while ~2.2 Sv of AABW rises from deeper layers (~4,500 m), revealing a vertically structured transformation of abyssal waters (Figure 3f). Farther north along the Somali margin, ~1 Sv of AABW upwells near ~4,500 m, while the overlying LCDW exhibits downwelling (Figure 3b), likely driven by the intrusion of dense Red Sea Overflow Waters. Secondary upwelling hotspots, also governed by topography, are distributed across the basin. Along the western and southern Australian margins, a vertically layered structure emerges, with ~0.5 Sv of LCDW downwelling above ~4,000 m and ~0.6 Sv of AABW upwelling near the bottom (Figure 3g). In the basin interior, strong upwelling is concentrated along fracture zones of the Southwest Indian Ridge, with ~3 Sv of LCDW and ~2.1 Sv of AABW (Figure 3d), while along the Ninety-East Ridge, ~1.1 Sv of AABW upwells (Figure 3e) beneath weak LCDW downwelling (~0.4 Sv).

Near the equator (±2.5°), ~2.05 Sv of abyssal water upwells around ~4,000 m (Figure 3c), consistent with enhanced mixing driven by nonlinear wave interactions (Delorme et al., 2021). This equatorial upwelling reflects a distinct dynamical regime, where wave-driven mixing dominates over topographically controlled upwelling elsewhere in the basin. Together, these results demonstrate that abyssal upwelling in the IO is highly localized and primarily controlled by topography, while also exhibiting regionally distinct dynamical regimes that govern the transformation of abyssal waters into the overlying lighter watermass.

3.4. Return Flow of Deep Water

In the IO basin, northward-propagating abyssal waters (AABW–LCDW) are progressively transformed into overlying deep waters, namely Indian Deep Water (IDW) and its upper circumpolar branch, Upper Circumpolar Deep Water (UCDW) (Figure 2c). Vertical volume flux diagnostics indicate that approximately ~10 Sv of abyssal transport is transferred upward within the basin into a thick deep layer spanning roughly 1,500–3,800 m, which forms the core of the IDW–UCDW return branch. These transformed deep waters subsequently organize into a coherent southward flow, primarily along boundary currents with additional contributions from interior zonal pathways (Figure 2b).

In the Somali Basin, intermediate-depth downwelling of Red Sea Overflow Waters (RSOW) forms modified-RSOW ($\sigma_2 > 36.5$ kg m^{-3}), which feeds a southward-flowing deep western boundary current. Concurrently, ~1 Sv of abyssal waters upwell into the deep layer, strengthening the flow at intermediate depths (~1,800–3,200 m). Downstream, this current bifurcates into an equatorial zonal branch (~0.5 Sv) and a continued southward boundary current. The equatorial branch feeds the Central Indian basin, carrying the signature of modified RSOW waters (Figure 2b), while modified deep waters from the coastal Bay of Bengal also contribute to this region. As a result, the Central Indian basin exhibits a mixture of Arabian Sea (high-salinity) and Bay of Bengal (low-oxygen) signatures and acts as a reservoir that sustains a deep zonal flow (~2 Sv) opposing the ITF.

The southward return flow is primarily organized along boundary currents, which account for the dominant share of the transport (Figure 2b). In the western Indian Ocean, strong transformation in the Madagascar and Mascarene basins generates ~5.2 Sv of southward transport as deep western boundary currents. In addition, a narrow eastern-boundary current in the Perth Basin carries ~1.5 Sv of modified IDW southward, providing a secondary pathway for basin-scale return. In the Mozambique Basin, shallowing topography induces localized overturning that re-directs a smaller fraction (~0.5 Sv) of northward abyssal transport into southward and eastward deep return, eventually rejoining with the Southern Ocean.

4. Conclusions and Discussions

In this study, we use a high-resolution, eddy-resolving ROMS simulation to investigate the deep circulation and trace the abyssal pathways of the lower limb of the IO-MOC. The IO-MOC exhibits a predominantly single-celled structure sustained by the large influx of LCDW and AABW from the Southern Ocean. These abyssal waters enter the Indian Ocean through three dynamically distinct routes along the Perth, Crozet, and Mozambique basins, collectively transporting ~12.5 Sv across 32°S, consistent with inverse-box observational estimates (Figure 2d). The terrain-following framework captures deep and abyssal flows along narrow ridges and fracture zones, consistent with recent field campaigns (Menezes et al., 2024). During their northward propagation, the gradual aging of abyssal waters and associated depletion of dissolved oxygen (Figure 3a) indicate limited ventilation away from their Antarctic source regions. These pathways are shaped by topography and include multiple cyclonic and anticyclonic recirculations, highlighting the role of ridges and basin geometry in steering abyssal transport.

Variations in the overturning streamfunction ($\overline{\psi}$) are linked to spatiotemporal undulations of isopycnals, which drive substantial vertical volume flux across the basin. The IO emerges as a strongly upwelling basin, with a total diagnosed abyssal upwelling of ∼10 Sv, exceeding previous radiocarbon-based estimates (Srinivasan et al., 2000). Upwelling hotspots are concentrated along western boundary regions, including southern Africa, eastern Madagascar, and the Somali Basin, and are also prominent within fracture zones of the Southwest Indian Ridge, where elevated diffusivities have been observed (Arvapalli et al., 2022; MacKinnon et al., 2008; Menezes et al., 2024, 2026). Along the western Australian margin, ROMS resolves weaker bottom-intensified upwelling (∼0.6 Sv), smaller than observational estimates for the Perth Basin (Sloyan, 2006), while coarser-resolution models typically underrepresent abyssal upwelling at comparable depths (Figure 3g). These differences highlight the importance of terrain-following coordinates and high spatial resolution in resolving bottom boundary layer processes and fracture-zone exchange (Figure 3). The upward mass transfer associated with these hotspots forms the core of the deep (IDW–UCDW) layer, which subsequently feeds the southward return branch.

The progressive reduction in transport from abyssal inflow to upward transformation and coherent southward return flow reflects the distributed and pathway-dependent nature of overturning within the IO. While ∼12.5 Sv of abyssal waters enter the basin, ∼10 Sv is transformed within spatially heterogeneous upwelling regions, and ∼8 Sv subsequently organizes into a coherent southward deep return flow. The remaining transport is redistributed through interior recirculation, lateral spreading, and localized exchanges across density layers, underscoring the role of topographic control and mixing processes in shaping the efficiency and structure of the overturning circulation. Building on the quantified upwelling and return pathways, these results provide a process-based framework for understanding the IO overturning system, identify previously unresolved pathways, regions of large-scale upwelling, and improve basin-scale transports. The present estimates represent a key step toward advancing the representation of abyssal overturning in climate models. This framework enables future studies to assess emerging evidence of a recent weakening in the ventilation of dissolved gases and abyssal transports (Gunn et al., 2023; Johnson & Purkey, 2024; Rintoul et al., 2026). It also opens new directions to further investigate the seasonal variability of pathways and to quantify the relative roles of diapycnal and isopycnal upwelling in setting the overturning structure.

Conflict of Interest

The authors declare no conflicts of interest relevant to this study.

Availability Statement

The OSCAR data set is publicly available at Dohan (2021). The GHRSST data can be accessed from Remote Sensing Systems (2017). The ESACCI SSS weekly data can be obtained from Boutin et al. (2019). The ECCOv4r4 and GLORYS12v1 monthly data sets are available at Fenty and Wang (2020) and CMEMS (2023), respectively. The JRA-55 river runoff data set can be downloaded from Japan Meteorological Agency, Japan (2013). The ROMS data to reproduce the figures in this manuscript and the accompanying Python scripts are available at Mishra (2025).

Acknowledgments
K.M. acknowledges the Prime Minister's Research Fellowship (PMRF). B.G. acknowledges support from ANRF Grant SPR/2020/000531. Numerical simulations were conducted on the Australian National Computational Infrastructure, which is supported by the Commonwealth of Australia, and the Supercomputer Education and Research Centre (SERC), which is supported by the Indian Institute of Science. The authors thank the Consortium for Ocean-Sea Ice Modeling in Australia (COSIMA; http://www.cosima.org.au) for making the ACCESS-OM2 suite of models available. Open access publishing facilitated by The University of Melbourne, as part of the Wiley - The University of Melbourne agreement via the Council of Australasian University Librarians. The authors thank Bajrang assistance in creating the schematic. They also thank Ben Galton-Fenzi and Shrikant for valuable discussions during the model setup.

References

Aguiar, W., Mata, M. M., & Kerr, R. (2017). On deep convection events and Antarctic bottom water formation in ocean reanalysis products. *Ocean Science*, *13*(6), 851–872. https://doi.org/10.5194/os-13-851-2017

Ansorge, I. J., Baringer, M., Campos, E. J., Dong, S., Fine, R., Garzoli, S. L., et al. (2014). Basin-wide oceanographic array bridges the South Atlantic. *EOS Transactions of the American Geophysical Union*, *95*(6), 53–54. https://doi.org/10.1002/2014EO060001

Aoki, S., Rintoul, S. R., Ushio, S., Watanabe, S., & Bindoff, N. L. (2005). Freshening of the Adélie land bottom water near 140 E. *Geophysical Research Letters*, *32*(23). https://doi.org/10.1029/2005GL024246

Arvapalli, S. R., Bajish, C., & Kurian, J. (2022). Hydrographic observations in the rift valley of southwest indian ridge from 63° e–69° e. *Dynamics of Atmospheres and Oceans*, *97*, 101284. https://doi.org/10.1016/j.dynatmoce.2022.101284

Bindoff, N. L., & Hobbs, W. R. (2013). Deep ocean freshening. *Nature Climate Change*, *3*(10), 864–865. https://doi.org/10.1038/nclimate2014

Boutin, J., Vergely, J. L., Koehler, J., Rouffi, F., & Reul, N. (2019). Esa sea surface salinity climate change initiative (sea_surface_salinity_cci): Weekly sea surface salinity product v1.*8*. https://doi.org/10.5285/9ef0ebf847564c2eabe62cac4899ec41

Budgell, W. (2005). Numerical simulation of ice-ocean variability in the Barents Sea region: Towards dynamical downscaling. *Ocean Dynamics*, *55*(3), 370–387. https://doi.org/10.1007/s10236-005-0008-3

Butler, E., Oliver, K., Hirschi, J. J.-M., & Mecking, J. (2016). Reconstructing global overturning from meridional density gradients. *Climate Dynamics*, *46*(7–8), 2593–2610. https://doi.org/10.1007/s00382-015-2719-6

Cessi, P. (2019). The global overturning circulation. *Annual Review of Marine Science*, *11*(1), 249–270. https://doi.org/10.1146/annurev-marine-010318-095241

Chapman, D. C. (1985). Numerical treatment of cross-shelf open boundaries in a barotropic coastal ocean model. *Journal of Physical Oceanography*, *15*(8), 1060–1075. https://doi.org/10.1175/1520-0485(1985)015⟨1060:NTOCSO⟩2.0.CO;2

CMEMS. (2023). *Global ocean physics reanalysis*. Mercator Océan International. https://doi.org/10.48670/moi-00021

Delorme, B. L., Thomas, L. N., Marchesiello, P., Gula, J., Roullet, G., & Molemaker, M. J. (2021). Enhanced abyssal mixing in the equatorial Pacific associated with non-traditional effects. *Journal of Physical Oceanography*, *51*(6), 1895–1914. https://doi.org/10.1175/JPO-D-20-0238.1

Dengler, M., Quadfasel, D., Schott, F., & Fischer, J. (2002). Abyssal circulation in the Somali basin. *Deep Sea Research Part II: Topical Studies in Oceanography*, *49*(7–8), 1297–1322. https://doi.org/10.1016/S0967-0645(01)00167-9

Dohan, K. (2021). *Ocean surface current analyses real-time (oscar) surface currents - Interim 0.25 degree (version 2.0)*. NASA Physical Oceanography Distributed Active Archive Center. https://doi.org/10.5067/OSCAR-25I20

Drijfhout, S. S., & Garabato, A. C. N. (2008). The zonal dimension of the Indian Ocean meridional overturning circulation. *Journal of Physical Oceanography*, *38*(2), 359–379. https://doi.org/10.1175/2007JPO3640.1

Droghei, R., Buongiorno Nardelli, B., & Santoleri, R. (2018). A new global sea surface salinity and density dataset from multivariate observations (1993–2016). *Frontiers in Marine Science*, *5*, 84. https://doi.org/10.3389/fmars.2018.00084

Durski, S. M., & Kurapov, A. L. (2019). A high-resolution coupled ice-ocean model of winter circulation on the Bering sea shelf. Part I: Ice model refinements and skill assessments. *Ocean Modelling*, *133*, 145–161. https://doi.org/10.1016/j.ocemod.2018.11.004

Ezer, T., & Mellor, G. L. (2004). A generalized coordinate ocean model and a comparison of the bottom boundary layer dynamics in terrain-following and in z-level grids. *Ocean Modelling*, *6*(3–4), 379–403. https://doi.org/10.1016/S1463-5003(03)00026-X

Fairall, C. W., Bradley, E. F., Hare, J., Grachev, A. A., & Edson, J. B. (2003). Bulk parameterization of air–sea fluxes: Updates and verification for the coare algorithm. *Journal of Climate*, *16*(4), 571–591. https://doi.org/10.1175/1520-0442(2003)016⟨0571:BPOASF⟩2.0.CO;2

Fenty, I., & Wang, O. (2020). *Ecco gent-mcwilliams ocean bolus velocity - Daily mean llc90 grid (version 4 release 4)*. NASA Physical Oceanography Distributed Active Archive Center. https://doi.org/10.5067/ECL5D-BOL44

Fieux, M., & Swallow, J. (1988). Flow of deep water into the Somali basin. Deep sea research Part A. *Oceanographic Research Papers*, *35*(2), 303–309. https://doi.org/10.1016/0198-0149(88)90041-6

Flather, R. (1976). A tidal model of the northwest European continental shelf. *Mem. Soc. Roy. Sci. Liege*, *10*, 141–164.

Forget, G., Campin, J.-M., Heimbach, P., Hill, C., Ponte, R., & Wunsch, C. (2015). ECCO version 4: An integrated framework for non-linear inverse modeling and global ocean state estimation. *Geoscientific Model Development*, *8*(10), 3071–3104. https://doi.org/10.5194/gmd-8-3071-2015

Foster, T. D., & Carmack, E. C. (1976). Temperature and salinity structure in the Weddell Sea. *Journal of Physical Oceanography*, *6*(1), 36–44. https://doi.org/10.1175/1520-0485(1976)006⟨0036:TASSIT⟩2.0.CO;2

Ganachaud, A., Wunsch, C., Marotzke, J., & Toole, J. (2000). Meridional overturning and large-scale circulation of the Indian Ocean. *Journal of Geophysical Research*, *105*(C11), 26117–26134. https://doi.org/10.1029/2000JC900122

Garcia, H., Wang, Z., Bouchard, C., Cross, S., Paver, C., & Reagan, J. (2024). World ocean atlas 2023. Volume 3: Dissolved oxygen, apparent oxygen utilization, dissolved oxygen saturation, and 30-year climate normal. https://doi.org/10.25923/rb67-ns53

GEBCO Compilation Group. (2022). GEBCO_2022 grid. https://doi.org/10.5285/e0f0bb80-ab44-2739-e053-6c86abc0289c

Gordon, A. L. (2009). Bottom water formation. *Ocean currents*, *263*, 269–421. https://doi.org/10.1016/B978-012374473-9.00006-0

Gunn, K. L., Rintoul, S. R., England, M. H., & Bowen, M. M. (2023). Recent reduced abyssal overturning and ventilation in the Australian Antarctic basin. *Nature Climate Change*, *13*(6), 537–544. https://doi.org/10.1038/s41558-023-01667-8

Haidvogel, D. B., & Beckmann, A. (1999). Numerical ocean circulation modeling. *World Scientific*. https://doi.org/10.1142/p097

Haynes, S. J., MacLeod, K. G., Ladant, J.-B., Guchte, A. V., Rostami, M. A., Poulsen, C. J., & Martin, E. E. (2020). Constraining sources and relative flow rates of bottom waters in the Late Cretaceous Pacific Ocean. *Geology*, *48*(5), 509–513. https://doi.org/10.1130/G47197.1

Hersbach, H., Bell, B., Berrisford, P., Hirahara, S., Horányi, A., Muñoz-Sabater, J., et al. (2020). The ERA5 global reanalysis. *Quarterly Journal of the Royal Meteorological Society*, *146*(730), 1999–2049. https://doi.org/10.1002/qj.3803

Hunke, E. C., & Dukowicz, J. K. (1997). An elastic–viscous–plastic model for sea ice dynamics. *Journal of Physical Oceanography*, *27*(9), 1849–1867. https://doi.org/10.1175/1520-0485(1997)027⟨1849:AEVPMF⟩2.0.CO;2

Japan Meteorological Agency, Japan. (2013). *Jra-55: Japanese 55-year reanalysis, daily 3-hourly and 6-hourly data*. Research Data Archive at the National Center for Atmospheric Research, Computational and Information Systems Laboratory. Retrieved from https://doi.org/10.5065/XYTB-VV76

Jean-Michel, L., Eric, G., Romain, B.-B., Gilles, G., Angélique, M., Marie, D., et al. (2021). The copernicus global 1/12 oceanic and sea ice GLORYS12 reanalysis. *Frontiers in Earth Science*, *9*, 698876. https://doi.org/10.3389/feart.2021.698876

Johns, W. E., Baringer, M. O., Beal, L., Cunningham, S., Kanzow, T., Bryden, H. L., et al. (2011). Continuous, array-based estimates of Atlantic Ocean heat transport at 26.5 N. *Journal of Climate*, *24*(10), 2429–2449. https://doi.org/10.1175/2010JCLI3997.1

Johnson, G. C. (2008). Quantifying antarctic bottom water and North Atlantic deep water volumes. *Journal of Geophysical Research*, *113*(C5). https://doi.org/10.1029/2007JC004477

Johnson, G. C., & Purkey, S. G. (2024). Refined estimates of global ocean deep and abyssal decadal warming trends. *Geophysical Research Letters*, *51*(18), e2024GL111229. https://doi.org/10.1029/2024GL111229

Kiss, A. E., Hogg, A. M., Hannah, N., Boeira Dias, F., Brassington, G. B., Chamberlain, M. A., et al. (2020). ACCESS-OM2 v1. 0: A global ocean–sea ice model at three resolutions. *Geoscientific Model Development*, *13*(2), 401–442. https://doi.org/10.5194/gmd-13-401-2020

Kuhlbrodt, T., Griesel, A., Montoya, M., Levermann, A., Hofmann, M., & Rahmstorf, S. (2007). On the driving processes of the Atlantic meridional overturning circulation. *Reviews of Geophysics*, *45*(2). https://doi.org/10.1029/2004RG000166

Kumar, R., Li, J., Hedstrom, K., Babanin, A. V., Holland, D. M., Heil, P., & Tang, Y. (2021). Intercomparison of Arctic sea ice simulation in ROMS-CICE and ROMS-Budgell. *Polar Science*, *29*, 100716. https://doi.org/10.1016/j.polar.2021.100716

Lee, T., & Marotzke, J. (1998). Seasonal cycles of meridional overturning and heat transport of the Indian Ocean. *Journal of Physical Oceanography*, *28*(5), 923–943. https://doi.org/10.1175/1520-0485(1998)028⟨0923:ScomOA⟩2.0.CO;2

Li, Z., Chao, Y., & McWilliams, J. C. (2006). Computation of the streamfunction and velocity potential for limited and irregular domains. *Monthly Weather Review*, *134*(11), 3384–3394. https://doi.org/10.1175/MWR3249.1

Lumpkin, R., & Speer, K. (2007). Global ocean meridional overturning. *Journal of Physical Oceanography*, *37*(10), 2550–2562. https://doi.org/10.1175/JPO3130.1

MacKinnon, J., Johnston, T. S., & Pinkel, R. (2008). Strong transport and mixing of deep water through the southwest Indian ridge. *Nature Geoscience*, *1*(11), 755–758. https://doi.org/10.1038/ngeo340

Mahieu, L., Lo Monaco, C., Metzl, N., Fin, J., & Mignon, C. (2020). Variability and stability of anthropogenic CO 2 in Antarctic bottom waters observed in the Indian sector of the Southern Ocean, 1978–2018. *Ocean Science Discussions*, 1–28. https://doi.org/10.5194/os-16-1559-2020

Mantyla, A. W., & Reid, J. L. (1995). On the origins of deep and bottom waters of the Indian Ocean. *Journal of Geophysical Research*, *100*(C2), 2417–2439. https://doi.org/10.1029/94JC02564

Marchesiello, P., McWilliams, J. C., & Shchepetkin, A. (2001). Open boundary conditions for long-term integration of regional oceanic models. *Ocean Modelling*, *3*(1–2), 1–20. https://doi.org/10.1016/S1463-5003(00)00013-5

Mashayek, A., Gula, J., Baker, L. E., Naveira Garabato, A. C., Cimoli, L., Riley, J. J., & De Lavergne, C. (2024). On the role of seamounts in upwelling deep-ocean waters through turbulent mixing. *Proceedings of the National Academy of Sciences*, *121*(27), e2322163121. https://doi.org/10.1073/pnas.2322163121

McDonagh, E. L., Bryden, H. L., King, B. A., & Sanders, R. J. (2008). The circulation of the Indian Ocean at 32 s. *Progress in Oceanography*, *79*(1), 20–36. https://doi.org/10.1016/j.pocean.2008.07.001

Mellor, G. L., & Yamada, T. (1982). Development of a turbulence closure model for geophysical fluid problems. *Reviews of Geophysics*, *20*(4), 851–875. https://doi.org/10.1029/RG020i004p00851

Menezes, V. V., Furey, H., Torres, D. J., Bahr, F., & Baker, L. (2026). Direct observations of strong jets transporting deep and bottom water into the Indian Ocean through the fracture zones of the southwest Indian ridge. *Journal of Geophysical Research: Oceans*, *131*(3), e2025JC023864. https://doi.org/10.1029/2025JC023864

Menezes, V. V., Robbins, P., Furey, H., & Mazloff, M. (2024). Deep argo observations of Antarctic bottom water in the deep fracture zones of the Southwest Indian Ridge. *Journal of Geophysical Research: Oceans*, *129*(7), e2024JC021165. https://doi.org/10.1029/2024JC021165

Mensah, V., Nakayama, Y., Fujii, M., Nogi, Y., & Ohshima, K. I. (2021). Dense water downslope flow and aabw production in a numerical model: Sensitivity to horizontal and vertical resolution in the region off cape darnley polynya. *Ocean Modelling*, *165*, 101843. https://doi.org/10.1016/j.ocemod.2021.101843

Mishra, K. (2025). Dataset for tracing the abyssal water pathways in the Indian Ocean [Dataset]. *Zenodo*. https://doi.org/10.5281/zenodo.15603225

Munk, W., & Wunsch, C. (1998). Abyssal recipes II: Energetics of tidal and wind mixing. *Deep Sea Research Part I: Oceanographic Research Papers*, *45*(12), 1977–2010. https://doi.org/10.1016/S0967-0637(98)00070-3

Onken, R. (1995). The spreading of lower circumpolar deep water in the Atlantic Ocean. *Journal of Physical Oceanography*, *25*(12), 3051–3063. https://doi.org/10.1175/1520-0485(1995)025⟨3051:TSOLCD⟩2.0.CO;2

Orsi, A. H., Jacobs, S. S., Gordon, A. L., & Visbeck, M. (2001). Cooling and ventilating the abyssal ocean. *Geophysical Research Letters*, *28*(15), 2923–2926. https://doi.org/10.1029/2001GL012830

Pacanowski, R. C., & Gnanadesikan, A. (1998). Transient response in a z-level ocean model that resolves topography with partial cells. *Monthly Weather Review*, *126*(12), 3248–3270. https://doi.org/10.1175/1520-0493(1998)126⟨3248:TRIAZL⟩2.0.CO;2

Purkey, S. G., & Johnson, G. C. (2010). Warming of global abyssal and deep Southern Ocean waters between the 1990s and 2000s: Contributions to global heat and sea level rise budgets. *Journal of Climate*, *23*(23), 6336–6351. https://doi.org/10.1175/2010JCLI3682.1

Purkey, S. G., & Johnson, G. C. (2013). Antarctic bottom water warming and freshening: Contributions to sea level rise, ocean freshwater budgets, and global heat gain. *Journal of Climate*, *26*(16), 6105–6122. https://doi.org/10.1175/JCLI-D-12-00834.1

Remote Sensing Systems. (2017). Ghrsst level 4 mw_ir_oi global foundation sea surface temperature analysis version 5.0 from remss. *NASA Physical Oceanography Distributed Active Archive Center*. https://doi.org/10.5067/GHMWI-4FR05

Richardson, P. L. (2008). On the history of meridional overturning circulation schematic diagrams. *Progress in Oceanography*, *76*(4), 466–486. https://doi.org/10.1016/j.pocean.2008.01.005

Rintoul, S. R., Stewart, A. L., Johnson, G. C., Zhou, S., Foppert, A., Li, Q., et al. (2026). Antarctic bottom water in a changing climate. *Nature Reviews Earth & Environment*, *7*(2), 86–102. https://doi.org/10.1038/s43017-025-00750-2

Robbins, P. E., & Toole, J. M. (1997). The dissolved silica budget as a constraint on the meridional overturning circulation of the Indian Ocean. *Deep Sea Research Part I: Oceanographic Research Papers*, *44*(5), 879–906. https://doi.org/10.1016/S0967-0637(96)00126-4

Schiermeier, Q. (2013). Oceans under surveillance. *Nature*, *497*(7448), 167–168. https://doi.org/10.1038/497167a

Silvano, A., Purkey, S., Gordon, A. L., Castagno, P., Stewart, A. L., Rintoul, S. R., et al. (2023). Observing Antarctic bottom water in the Southern Ocean. *Frontiers in Marine Science*, *10*, 1221701. https://doi.org/10.3389/fmars.2023.1221701

Sloyan, B. M. (2006). Antarctic bottom and lower circumpolar deep water circulation in the eastern Indian Ocean. *Journal of Geophysical Research*, *111*(C2). https://doi.org/10.1029/2005JC003011

Sloyan, B. M., & Rintoul, S. R. (2001). The southern ocean limb of the global deep overturning circulation. *Journal of Physical Oceanography*, *31*(1), 143–173. https://doi.org/10.1175/1520-0485(2001)031⟨0143:TSOLOT⟩2.0.CO;2

Solodoch, A., Stewart, A., Hogg, A. M., Morrison, A., Kiss, A., Thompson, A., et al. (2022). How does antarctic bottom water cross the southern ocean? *Geophysical Research Letters*, *49*(7), e2021GL097211. https://doi.org/10.1029/2021GL097211

Spall, M. A. (2024). An overlooked component of the meridional overturning circulation. *Journal of Physical Oceanography*, *54*(9), 1921–1932. https://doi.org/10.1175/JPO-D-24-0019.1

Srinivasan, A., Garraffo, Z., & Iskandarani, M. (2009). Abyssal circulation in the Indian Ocean from a 1/12° resolution global hindcast. *Deep Sea Research Part I: Oceanographic Research Papers*, *56*(11), 1907–1926. https://doi.org/10.1016/j.dsr.2009.07.001

Srinivasan, A., Rooth, C. G., Top, Z., & Olson, D. (2000). Abyssal upwelling in the Indian Ocean: Radiocarbon diagnostics. *Journal of Marine Research*, *58*(5), 755–778. https://doi.org/10.1357/002224000321358891

Talley, L. D. (2013). Closure of the global overturning circulation through the Indian, Pacific, and Southern Oceans: Schematics and transports. *Oceanography*, *26*(1), 80–97. https://doi.org/10.5670/oceanog.2013.07

Tang, Y. M., & Roberts, M. J. (2005). The impact of a bottom boundary layer scheme on the North Atlantic Ocean in a global coupled climate model. *Journal of Physical Oceanography*, *35*(2), 202–217. https://doi.org/10.1175/jpo-2671.1

van Aken, H. M., Ridderinkhof, H., & de Ruijter, W. P. (2004). North Atlantic deep water in the south-western Indian Ocean. *Deep Sea Research Part I: Oceanographic Research Papers*, *51*(6), 755–776. https://doi.org/10.1016/j.dsr.2004.01.008

Warren, B. A. (1974). Deep flow in the Madagascar and mascarene basins. *Deep-Sea Research and Oceanographic Abstracts*, *21*, 1–21. https://doi.org/10.1016/0011-7471(74)90015-1

Winton, M., Hallberg, R., & Gnanadesikan, A. (1998). Simulation of density-driven frictional downslope flow in z-coordinate ocean models. *Journal of Physical Oceanography*, *28*(11), 2163–2174. https://doi.org/10.1175/1520-0485(1998)028⟨2163:SODDFD⟩2.0.CO;2

Zhou, J., Li, Y., Du, Y., Hong, Y., Lu, L., Lu, Y., et al. (2024). Indian Ocean intermediate water masses and their simulations by cmip6 models. *Journal of Climate*, *37*(23), 6285–6303. https://doi.org/10.1175/JCLI-D-23-0667.1

References From the Supporting Information

Budgell, W. (2005). Numerical simulation of ice-ocean variability in the Barents Sea region: Towards dynamical downscaling. *Ocean Dynamics*, *55*(3), 370–387. https://doi.org/10.1007/s10236-005-0008-3

Chapman, D. C. (1985). Numerical treatment of cross-shelf open boundaries in a barotropic coastal ocean model. *Journal of Physical Oceanography*, *15*(8), 1060–1075. https://doi.org/10.1175/1520-0485(1985)015⟨1060:NTOCSO⟩2.0.CO;2

Droghei, R., Buongiorno Nardelli, B., & Santoleri, R. (2018). A new global sea surface salinity and density dataset from multivariate observations (1993–2016). *Frontiers in Marine Science*, *5*, 84. https://doi.org/10.3389/fmars.2018.00084

Durski, S. M., & Kurapov, A. L. (2019). A high-resolution coupled ice-ocean model of winter circulation on the Bering sea shelf. Part I: Ice model refinements and skill assessments. *Ocean Modelling*, *133*, 145–161. https://doi.org/10.1016/j.ocemod.2018.11.004

Fairall, C. W., Bradley, E. F., Hare, J., Grachev, A. A., & Edson, J. B. (2003). Bulk parameterization of air–sea fluxes: Updates and verification for the coare algorithm. *Journal of Climate*, *16*(4), 571–591. https://doi.org/10.1175/1520-0442(2003)016⟨0571:BPOASF⟩2.0.CO;2

Flather, R. (1976). A tidal model of the northwest European continental shelf. *Mem. Soc. Roy. Sci. Liege*, *10*, 141–164.

GEBCO Compilation Group. (2022). GEBCO_2022 grid. https://doi.org/10.5285/e0f0bb80-ab44-2739-e053-6c86abc0289c

Haidvogel, D. B., & Beckmann, A. (1999). Numerical ocean circulation modeling. *World Scientific*. https://doi.org/10.1142/p097

Hersbach, H., Bell, B., Berrisford, P., Hirahara, S., Horányi, A., Muñoz-Sabater, J., et al. (2020). The ERA5 global reanalysis. *Quarterly Journal of the Royal Meteorological Society*, *146*(730), 1999–2049. https://doi.org/10.1002/qj.3803

Hunke, E. C., & Dukowicz, J. K. (1997). An elastic–viscous–plastic model for sea ice dynamics. *Journal of Physical Oceanography*, *27*(9), 1849–1867. https://doi.org/10.1175/1520-0485(1997)027⟨1849:AEVPMF⟩2.0.CO;2

Kumar, R., Li, J., Hedstrom, K., Babanin, A. V., Holland, D. M., Heil, P., & Tang, Y. (2021). Intercomparison of Arctic sea ice simulation in ROMS-CICE and ROMS-Budgell. *Polar Science*, *29*, 100716. https://doi.org/10.1016/j.polar.2021.100716

Li, Z., Chao, Y., & McWilliams, J. C. (2006). Computation of the streamfunction and velocity potential for limited and irregular domains. *Monthly Weather Review*, *134*(11), 3384–3394. https://doi.org/10.1175/MWR3249.1

Marchesiello, P., McWilliams, J. C., & Shchepetkin, A. (2001). Open boundary conditions for long-term integration of regional oceanic models. *Ocean Modelling*, *3*(1–2), 1–20. https://doi.org/10.1016/S1463-5003(00)00013-5

Mellor, G. L., & Kantha, L. (1989). An ice-ocean coupled model. *Journal of Geophysical Research*, *94*(C8), 10937–10954. https://doi.org/10.1029/JC094iC08p10937

Reagan, J. R., Boyer, T. P., García, H. E., Locarnini, R. A., Baranova, O. K., Bouchard, C., et al. (2023). World Ocean Atlas 2023 [Dataset]. *NOAA National Centers for Environmental Information*. https://doi.org/10.25921/va26-hv25

Shchepetkin, A. F., & McWilliams, J. C. (2005). The regional oceanic modeling system (ROMS): A split-explicit, free-surface, topography-following-coordinate oceanic model. *Ocean Modelling*, *9*(4), 347–404. https://doi.org/10.1016/j.ocemod.2004.08.002

Sprintall, J., Wijffels, S. E., Molcard, R., & Jaya, I. (2009). Direct estimates of the Indonesian Throughflow entering the Indian Ocean: 2004–2006. *Journal of Geophysical Research*, *114*(C7). https://doi.org/10.1029/2008JC005257

Suzuki, T., Yamazaki, D., Tsujino, H., Komuro, Y., Nakano, H., & Urakawa, S. (2018). A dataset of continental river discharge based on JRA-55 for use in a global ocean circulation model. *Journal of Oceanography*, *74*(4), 421–429. https://doi.org/10.1007/s10872-017-0458-5

Zhang, T., Wang, W., Xie, Q., Liu, K., Wang, D., Wu, X., et al. (2021). A new presentation of the Indian Ocean shallow overturning circulation from a vertical perspective. *Atmospheric and Oceanic Science Letters*, *14*(5), 100061. https://doi.org/10.1016/j.aosl.2021.100061